

Nuclear Science and Engineering

ISSN: (Print) (Online) Journal homepage: www.tandfonline.com/journals/unse20

On the Application of the Nyström Method to Two-Dimensional Neutral Particle Transport Problems in Heterogeneous Media

Gustavo A. Lorensi, Leonardo R. C. Moraes, Richard Vasques, Esequia Sauter & Fábio S. de Azevedo

To cite this article: Gustavo A. Lorensi, Leonardo R. C. Moraes, Richard Vasques, Esequia Sauter & Fábio S. de Azevedo (20 May 2024): On the Application of the Nyström Method to Two-Dimensional Neutral Particle Transport Problems in Heterogeneous Media, Nuclear Science and Engineering, DOI: 10.1080/00295639.2024.2342498

To link to this article: https://doi.org/10.1080/00295639.2024.2342498

Published online: 20 May 2024.

Submit your article to this journal

View related articles

View Crossmark data

Full Terms & Conditions of access and use can be found at
https://www.tandfonline.com/action/journalInformation?journalCode=unse20

NUCLEAR SCIENCE AND ENGINEERING
© 2024 American Nuclear Society
DOI: https://doi.org/10.1080/00295639.2024.2342498

Check for updates

On the Application of the Nyström Method to Two-Dimensional Neutral Particle Transport Problems in Heterogeneous Media

Gustavo A. Lorensi,[a]* Leonardo R. C. Moraes,[b] Richard Vasques,[b] Esequia Sauter,[a] and Fábio S. de Azevedo[a]

[a]*Universidade Federal do Rio Grande do Sul, Instituto de Matemática e Estatística, Av. Bento Gonçalves, P.O. Box 15080, 91509-900, Porto Alegre, RS, Brazil*
[b]*The Ohio State University, Department of Mechanical and Aerospace Engineering, 201 West 19th Avenue, Columbus, Ohio 43210*

Received December 12, 2023
Accepted for Publication April 3, 2024

Abstract — *Over time, several methods were developed to deal with neutral particle transport problems. The interest in these problems is related to their wide range of applications, from neutron transport and heat transfer in nuclear reactors to radiative transfer in atmospheric clouds. Unlike the discrete ordinates or discrete ordinates–like methods, integral methods do not require discretization of angular variables. Instead, angular variables are completely eliminated by an integration procedure over the solid angle, which allows elimination of the ray effect. That said, this paper presents a new approach to estimate the scalar flux in two-dimensional fixed-source neutron transport problems in a heterogeneous medium, considering isotropic scattering and vacuum and reflective boundary conditions. Here, the Nyström method is combined with the singularity-subtraction technique to present an integral formulation for the scalar flux in a mesh grid over all regions of the domain. The iterative method of the Neumann series is used as an alternative to direct methods to solve the resulting system of equations generated from the domain discretization. Numerical results are given to verify the offered method.*

Keywords — *Neutron transport problems, X, Y geometry, integral formulation, Nyström method.*

Note — *Some figures may be in color only in the electronic version.*

I. INTRODUCTION

The transport equation is a conventional mathematical model used to model the migration of small particles, such as neutrons and photons, in a background material. It provides a clear picture of this complex system, representing a balance between the gains and losses of particles in the medium. This mathematical model has a wide range of applications such as neutron transport in nuclear reactors, radiation transport in gas turbines, and photon radiotherapy. Obtaining accurate results for the transport equation yields new experiments with high success rates, which decreases financial and human costs and increases safety in the production, development, and improvement of technologies.

Over the years, a considerable number of articles and other works dealing with the solution of the transport equation were produced using several methods, for instance, discrete ordinates (S_N)[1,2] and integral methods.[3–5] These methods differ mainly in how they deal with the integral term in the transport equation. The first one consists of discretizing the angular variable in N discrete directions and approximating the integral term making use of angular quadrature sets. This leads to a coupled system of ordinary differential equations with respect to the angular variable known as S_N transport equations. Different methods have been proposed to deal with S_N transport problems, such as the fine-mesh

*E-mail: gustavo.lorensi@hotmail.com

Diamond Difference method[6] and the coarse-mesh Analytical Discrete Ordinates (ADO) method described by Barichello and Siewert[7] and the Spectral Green's Function method by Barros and Larsen.[8]

It is known in the literature that discrete ordinates–based methods may display, in some problems, computational anomalies called ray effects originating from discretization of angular variables.[9] On the other hand, integral methods are known for mitigating ray effects.[10] This is because these methods consist of writing the integral formulation of the transport equation. Therefore, following integral methods, we do not need to deal directly with angular variables since they are eliminated by the process of integration over the solid angle.

A two-dimensional neutral particle transport problem was studied by Loyalka and Tsai, who in 1975 and 1976 published a series of works on the integral methods.[3,11] In Part II[11] and Part III[3] of the series, they applied the Nyström method to two-dimensional homogeneous problems with and without reflective boundary conditions. In such works, numerical results were presented, and they concluded that this approach is valid because it avoids the ray effect. More recently, this approach has been used by several authors in different problems: two-dimensional problems in a homogeneous domain,[5] one-dimensional problems in a heterogeneous domain,[12] and finite cylindrical problems in a homogeneous domain.[13]

The Nyström method is a well-established approach for the solution of integral equations. This method consists of rewriting the transport equation using its integral form and then replacing the integral operator with a quadrature numerical scheme and producing a linear system to be solved.[14] However, there is still a lack of publications regarding the application of integral methods in heterogeneous media, which is the goal of this work.

Based on this, we present in Sec. II an extension of the Nyström method to deal with steady-state, monoenergetic, two-dimensional neutral particle problems in a heterogeneous medium considering isotropic scattering and vaccum and reflective boundary conditions. The description of the numerical technique and implementation details of this method are presented in Secs. III and IV, respectively, where we describe the use of the singularity-subtraction technique to prevent numerical oscillation in the results and the use of the Neumann series for solving the resulting linear system. The coarse-mesh Response Matrix–Constant Nodal (RM-CN) method was also implemented to generate comparison results and study new problems. A brief description of this method and its implementation is described in Sec. V. Section VI presents numerical results with respect to four model problems to verify the accuracy of the offered method, and Sec. VII presents a number of concluding remarks and suggestions for future work.

At this point, we remark that an earlier version of this paper was presented at the 2023 International Conference on Mathematics and Computational Methods Applied to Nuclear Science and Engineering and was published in the meeting proceedings.[15]

II. INTEGRAL FORMULATION

Here, the steady-state monoenergetic problem in a heterogeneous, nonmultiplying medium with isotropic scattering and an isotropic source is considered. The linear Boltzmann equation in this case appears as

$$\Omega \cdot \nabla \Psi(\mathbf{x},\Omega) + \sigma_t(\mathbf{x})\Psi(\mathbf{x},\Omega) = \frac{\sigma_s(\mathbf{x})}{4\pi}\int_{S^2}\Psi(\mathbf{x},\Omega')d\Omega' + S(\mathbf{x}) \ , \qquad (1)$$

where $\mathbf{x} = (x_1, x_2, x_3) \in D \times \mathbb{R}$, $D = [0,a] \times [0,b]$; $\Omega \in S^2$ = two-dimensional unit sphere in $\mathbb{R}^3$ (see Ref. [6]); Ψ = neutron angular flux such that $\Psi(\mathbf{x},\Omega) = \frac{\partial \Psi}{\partial x_1}\vec{i} + \frac{\partial \Psi}{\partial x_2}\vec{j}$; $S(\mathbf{x}) = [0,a_s] \times [0,b_s]$ = internal isotropic neutron source; $\sigma_t(\mathbf{x})$ and $\sigma_s(\mathbf{x})$ = total and scattering macroscopic cross sections, respectively.

The spatial domain D considered in this work is composed of the union of nonoverlapping regions R_i (with $i = 1:4$, namely, Fig. 1) with region R_1 containing

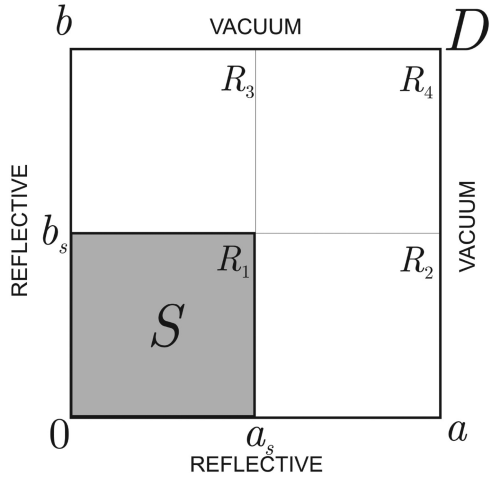


Fig. 1. Representation of domain D, where the R_i values are subregions of D and where S is the internal isotropic source.

the neutron source. The neutron source and cross sections are considered spatially uniform inside regions R_i.

To complete the statement of the problem, we impose vacuum boundary conditions on the right and top boundaries of the domain and reflective boundary conditions on the left and bottom boundaries of the domain. The boundary conditions are given by

$$\Psi(\mathbf{x},\Omega) = \beta\Psi(\mathbf{x},\Omega'), \quad \mathbf{n}\cdot\Omega < 0, \quad \mathbf{x}\in\partial D\times\mathbb{R} \ , \tag{2}$$

where $\beta = 0$ if $\mathbf{x}$ is in the left or top boundaries and $\beta = 1$ if $\mathbf{x}$ is in the bottom or right boundaries; $\Omega' = \Omega - 2(\mathbf{n}\cdot\Omega)\mathbf{n}$ = reflection of Ω on the boundary; $\mathbf{n}$ = outer unit normal vector. Now, in order to proceed, let us define the scalar flux as

$$\Phi(\mathbf{x}) = \frac{1}{4\pi}\int_{S^2}\Psi(\mathbf{x},\Omega)\,d\Omega \ . \tag{3}$$

Representing the right-hand side of Eq. (1) as $Q(x)$, applying the method of characteristics,[16] and integrating over the unitary sphere, the scalar flux can be written as

$$\Phi(\mathbf{x}) = \frac{1}{4\pi}\int_{S^2}\int_0^{s(\mathbf{x},\Omega)} Q(\mathbf{x}-r\Omega)e^{-\int_0^r \sigma_t(\mathbf{x}-s\Omega)ds} dr d\Omega \ , \tag{4}$$

where $s(\mathbf{x},\Omega) = \sup_{s>0}\{s : \mathbf{x}-s\Omega\in D\times\mathbb{R}\}$. Note that the integration interval of this last integral is equivalent to $D\times\mathbb{R}$. Because of the symmetry of $\mathbb{R}$, it is possible to change the integration interval and simplify this integration. Applying the change of variables $y = x - r\Omega$ and using the relation $dy = r^2 dr d\Omega$, the following expression is obtained:

$$\Phi(\mathbf{x}) = \frac{1}{2\pi}\int_0^\infty\int_D Q(\mathbf{y})\frac{e^{-\Lambda(\mathbf{x},\mathbf{y})}}{|\mathbf{x}-\mathbf{y}|^2}d\mathbf{y} \ , \tag{5}$$

where the function $\Lambda : D\times D\to\mathbb{R}_+$ is given by $\Lambda(\mathbf{x},y) = |\mathbf{x}-\mathbf{y}|_2\int_0^1\sigma_t((1-t)\mathbf{x}+t\mathbf{y})dt$ with $|\mathbf{x}-\mathbf{y}|_2 = \sqrt{(x_1-y_1)^2+(x_2-y_2)^2}$.

Defining the cosine of the elevation angle η as

$$\eta = \frac{\sqrt{(x_1-y_1)^2+(x_2-y_2)^2}}{\sqrt{(x_1-y_1)^2+(x_2-y_2)^2+(x_3-y_3)^2}} = \frac{|\mathbf{x}-\mathbf{y}|_2}{|\mathbf{x}-\mathbf{y}|} \tag{6}$$

and substituting this expression into Eq. (5), we obtain

$$\begin{aligned}\Phi(\mathbf{x}) &= \frac{1}{2\pi}\int_0^1\int_D Q(\mathbf{y})\frac{e^{-\frac{\Lambda(\mathbf{x},\mathbf{y})}{\eta}}}{\sqrt{1-\eta^2}|\mathbf{x}-\mathbf{y}|_2}dy_1dy_2d\eta \\ &= \frac{1}{2\pi}\int_D\frac{Q(\mathbf{y})}{|\mathbf{x}-\mathbf{y}|_2}\int_0^1\frac{e^{-\frac{\Lambda(\mathbf{x},\mathbf{y})}{\eta}}}{\sqrt{1-\eta^2}}d\eta dy_1dy_2 \\ &= \int_D Q(\mathbf{y})k(\mathbf{x},\mathbf{y})d\mathbf{y}\end{aligned} \tag{7}$$

where

$$k(\mathbf{x},\mathbf{y}) = \frac{1}{2\pi}\frac{1}{|\mathbf{x}-\mathbf{y}|_2}\int_0^1\frac{e^{-\frac{\Lambda(\mathbf{x},\mathbf{y})}{\eta}}}{\sqrt{1-\eta^2}}d\eta = \frac{1}{2\pi}\frac{Ki_1(\Lambda(\mathbf{x},\mathbf{y}))}{|\mathbf{x}-\mathbf{y}|_2} \ , \tag{8}$$

where Ki_1 represents the first-order Bickley-Naylor function.[17,18] To simplify the notation, define the integral operator L_g as follows:

$$(L_gQ)(\mathbf{x}) = \int_D Q(\mathbf{y})k(\mathbf{x},\mathbf{y})d\mathbf{y} \ . \tag{9}$$

Using the definition of $Q(\mathbf{x})$, and Eq. (7), it is possible to express the scalar flux as

$$\Phi(\mathbf{x}) = L_g(\sigma_s\Phi(\mathbf{x}) + S(\mathbf{x})) \ , \tag{10}$$

which is equivalent to

$$(1 - L_g\sigma_s)\Phi(x) = L_gS(\mathbf{x}) \ . \tag{11}$$

This operational equation has a solution Φ whenever the operator $1 - L_g\sigma_s$ is invertible. Because $\| L_g\sigma_s \| < 1$ in $L^2(D)$ and $L^\infty(D)$ spaces, when $\sigma_s < \sigma_c$, where σ_c is the inverse of the largest eigenvalue of L_g in $L^2(D)$,[19] the operator is invertible, and this last equation can be rewritten as

$$\Phi(\mathbf{x}) = (1 - L_g\sigma_s)^{-1}L_gS(\mathbf{x}) \ . \tag{12}$$

III. NUMERICAL TECHNIQUES

In order to produce accurate numerical results using the Nyström method, two factors must be taken into

consideration: the singularity of the operator L_g defined in Eq. (9) and the computation of the scalar flux in Eq. (12).

For the first consideration, one can notice that the operator L_g has a singularity when $\mathbf{x} = \mathbf{y}$ due to the kernel $k(\mathbf{x}, \mathbf{y})$. This means that when $\mathbf{x} = \mathbf{y}$, the denominator will be equal to zero, which creates a mathematical indetermination. Therefore, during the numerical integration over the variable $\mathbf{y}$, numerical oscillations will occur once $\mathbf{x}$ gets closer to $\mathbf{y}$. Because of this, the classical singularity subtraction technique[20] was used to attenuate such error. This technique consists of adding and subtracting the integrand from the integral and rearranging the terms properly; i.e., Eq. (9) can be rewritten as

$$\begin{aligned}\int_D Q(\mathbf{y})k(\mathbf{x},\mathbf{y})d\mathbf{y} &= \int_D Q(\mathbf{y})k(\mathbf{x},\mathbf{y}) + Q(\mathbf{x})k(\mathbf{x},\mathbf{y}) \\ &\quad - Q(\mathbf{x})k(\mathbf{x},\mathbf{y})d\mathbf{y} \\ &= \int_D (Q(\mathbf{y}) - Q(\mathbf{x}))k(\mathbf{x},\mathbf{y})d\mathbf{y} \\ &\quad + Q(\mathbf{x})\int_D k(\mathbf{x},\mathbf{y})d\mathbf{y} \quad . \end{aligned} \tag{13}$$

For a medium divided into multiple regions, it is possible to rewrite the operator as

$$\begin{aligned}(L_g Q)(\mathbf{x}) &= \sum_{R\in D:\mathbf{x}\in R}\int_R (Q(\mathbf{y}) - Q(\mathbf{x}))k(\mathbf{x},\mathbf{y})d\mathbf{y} \\ &\quad + \sum_{R\in D:\mathbf{x}\notin R}\int_R Q(\mathbf{y})k(\mathbf{x},\mathbf{y})d\mathbf{y} \\ &\quad + Q(\mathbf{x})\sum_{R\in D:\mathbf{x}\in R}\int_R k(\mathbf{x},\mathbf{y})d\mathbf{y} \quad . \end{aligned} \tag{14}$$

However, depending on the size of the region, numerical impressions can occur. This situation is explained by the fact that in some cases, the subtraction in Eq. (14) is applied even for $\mathbf{y}$, which is far from $\mathbf{x}$. Thus, one alternative to increasing the numerical precision is to decrease the size of the region in which the technique is being applied.

Thus, a discretization technique is applied to reduce the domain of integration. This concept is based on the idea of refining each part of the domain into smaller regions N_R, as shown in Figs. 2, 3, and 4. The original domain is said to be $N_R = 2$ because the interval $[0, a]$ was divided into two segments, as represented in Fig. 2. Each region in Fig. 2 can be divided into two regions, as represented in Fig. 3. These new regions inherit the characteristics of their respective region in Fig. 2, and it is said that $N_R = 4$ for this domain. The domain can also be divided in more regions, as represented in Fig. 4, where $N_R = 10$, and so on for any desired number of subregions.

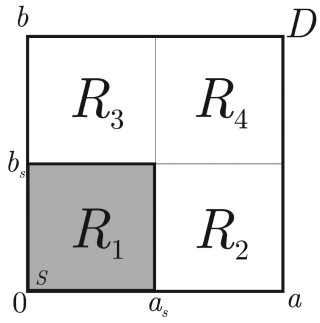


Fig. 2. Division of domain D into $N_R = 2$ subregions.

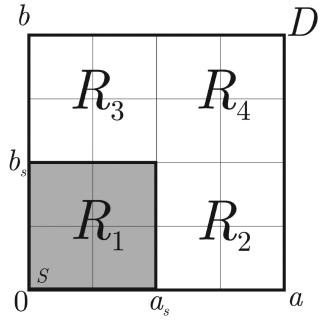


Fig. 3. Division of domain D into $N_R = 4$ subregions.

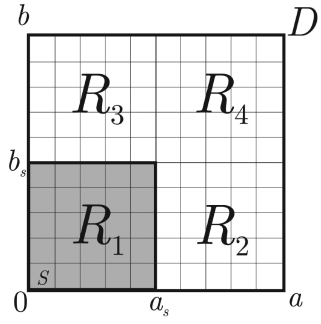


Fig. 4. Division of domain D into $N_R = 10$ subregions.

Combining this approach with the singularity-subtraction technique described by Eq. (14) results in integration over small regions. Integration over smaller regions requires less computational effort to be obtained and allows more precise numerical results.

In order to compute the scalar flux in Eq. (12), first the integrals in Eq. (14) must be calculated numerically. The Nyström method can be used for this. The method consists of replacing the integral of Eq. (14) by a selected numerical quadrature scheme. Applying this method, the previous equation can be written as

$$(L_g Q)(x_{ij}) = \sum_{R\in D: x_{ij}\notin R} \sum_{x_{ij}\neq x_{pq}} w_{pq} k(x_{ij}, x_{pq}) Q(x_{pq}) + \sum_{R\in D: x_{ij}\in R} \sum_{x_{ij}\neq x_{pq}} w_{pq} k(x_{ij}, x_{pq}) (Q(x_{pq}) - Q(x_{ij})) + Q(\mathbf{x}) K_{ij} \quad , \tag{15}$$

where x_{pq} and w_{pq}, $1 \le p \le M$ and $1 \le q \le M$, = nodes and weights of a numerical quadrature of size M, respectively; $K_{ij} = \sum_{R\in D:\mathbf{x}\in R} \int_R k(x_{ij}, \mathbf{y}) d\mathbf{y}$ with $k(x_{ij}, \mathbf{y})$ given in Eq. (8).

The approximated scalar flux in a mesh point can be obtained by solving the linear system in Eq. (11) discretized in a mesh. The discrete version of $(L_g Q)(x_{ij})$ produces a matrix of order M^4 that, in some cases, can increase processing time and lead to problems with computational storage. Thus, in order to avoid those situations, iterative methods can be used as an alternative to direct solvers.

Iterative methods attempt to solve linear systems by progressively iterating over an initial guess until a stopping criterion is achieved. These methods are more efficient in terms of memory usage and computational resources when compared to direct solvers since they require the storage of intermediate results at only each iteration rather than the complete solution matrix. Thus, the iterative process of the Neumann series was chosen because of its stability and low memory cost.[21] In this case, the scalar flux at any point can be written as

$$\Phi(\mathbf{x}) = \sum_{n=0}^{\infty} \sigma_s^n L_g^n (L_g S(\mathbf{x})) \quad . \tag{16}$$

However, as mentioned previously, the kernel of the L_g operator has singularity; see Eq. (8). Therefore, as a way to obtain more stable numerical results, the singularity subtraction technique, Eq. (14), can be applied to each L_g term in the previous equation. Thus, the previous series can be expanded and truncated with the scalar flux in a mesh written as

$$\Phi(\mathbf{x}_{ij}) \approx \sum_{n=0}^{m} \sigma_s^n T_{ij}^n + \frac{\sigma_s^{m+1}\sigma_c}{1-\sigma_s\sigma_c} T_{ij}^m \quad , \tag{17}$$

where

$$T_{ij}^0 = \sum_{R\in\mathcal{R}:\mathbf{x}_{ij}\notin R} \int_R k(x_{ij}, \mathbf{y}) S(\mathbf{y}) d\mathbf{y} + \sum_{R\in\mathcal{R}:\mathbf{x}_{ij}\in R} \int_R k(x_{ij}, \mathbf{y}) (S(\mathbf{y}) - S(x_{ij})) d\mathbf{y} + Q(x_{ij}) K_{ij} \tag{18a}$$

$$T_{ij}^{n+1} = \sum_{R\in D: x_{ij}\notin D} \sum_{p,q} w_{pq} k(x_{ij}, x_{pq}) T_{pq}^n + \sum_{R\in D: x_{ij}\in R} \sum_{x_{ij}\neq x_{pq}} w_{pq} \left[T_{pq}^n - T_{ij}^n\right] k(x_{ij}, x_{pq}) + T_{ij}^n K_{ij}, n \ge 0 \tag{18b}$$

and $1/\sigma_c$ is approximated by the Rayleigh quotient[19]

$$1/\sigma_c \approx \frac{< T_{ij}^{m-1}, T_{ij}^m >}{< T_{ij}^{m-1}, T_{ij}^{m-1} >} \quad , \tag{19}$$

where $< \mathbf{u}, \mathbf{v} >$ is the inner product of functions in L^2.

IV. IMPLEMENTATION DETAILS

Although the algorithm essentially consists of calculating the summation presented in Eq. (17) using the iterative procedure described in Eq. (18), several techniques were used in order to speed up the computer program running time and produce more accurate results.

First, the Bickley-Naylor function and the term K_{ij} are accessed several times during the execution, so calculating them for the same point multiple times is inefficient. Instead, those functions are tabulated over a fine mesh, and the code performs an interpolation in case there is a need for a point out of the mesh.

Another task with high computational cost is computing the terms of the Neumann series, i.e., Eq. (18). To minimize the computational running time spent in this calculation, the tabulation was parallelized with OpenMP,[22] an API that allows the distribution of activities to each of the threads of the same CPU in a shared memory computer. The tasks were dynamically distributed among the threads. As soon as a thread finishes processing a mesh point, it already receives another point so that there is no idle thread. Therefore, during iteration n, the mesh can be divided over the cores of a CPU since there is no dependence from any term of this iteration, just from the terms of the previous iteration, as can be noticed in Eq. (18b), where the term T^{n+1} depends only on T^n.

V. RM-CN METHOD

The RM-CN method is described in this article due to its role as a benchmark for the comparative analysis of numerical results, in contrast to the Nyström method, for problems that have not been documented in the existing literature. This approach was chosen because it is a well-known method to solve S_N transport problems and can be easily implemented. A more detailed

explanation of the RM-CN method can be found in Refs. [23–25].

First, define a spatial grid on the rectangular domain D, where each spatial node Γ_{ij} has width h_{x_i} and height h_{y_j}, $i = 1:I, j = 1:J$. The steady-state, monoenergetic, X,Y-geometry neutron transport equation in the S_N formulation appears as[6]

$$\begin{aligned}&\mu_m \frac{d}{dx}\psi_m(x,y) + \eta_m \frac{d}{dy}\psi_m(x,y) + \sigma_t^{ij}\psi_m(x,y)\\ &\quad = \frac{1}{4}\sum_{n=1}^{M}\sigma_s^{ij}\omega_n\psi_n(x,y) + Q^{ij},\\ &\quad m = 1:M, (x,y) \in \Gamma_{ij} \quad ,\end{aligned} \tag{20}$$

where N = order of the discrete ordinates formulation; $M = N(N+2)/2$ = number of discrete directions; μ_m and η_m = discrete directions of motion; ω_n = corresponding weights of the angular quadrature; σ_t^{ij} and σ_s^{ij} = total and scattering macroscopic cross sections, respectively; Q^{ij} = isotropic neutron source; $\psi_m(x,y)$ = angular flux in angular direction (μ_m, η_m) at (x,y). The cross sections and source are considered spatially uniform inside nodes Γ_{ij}.

Now, consider the following transverse-integrated fluxes over x-coordinate and y-coordinate directions:

$$\widetilde{\Psi}_m^j(x) = \frac{1}{h_{y_j}}\int_{y_j}^{y_{j+1}} \Psi_m(x,y)dy \tag{21}$$

$$\widehat{\Psi}_m^i(y) = \frac{1}{h_{x_i}}\int_{x_i}^{x_{i+1}} \Psi_m(x,y)dx \quad , \tag{22}$$

where $\widetilde{\Psi}_m^j(x)$ = node-edge average angular flux along the y direction; $\widehat{\Psi}_m^i(y)$ = node-edge average angular flux along the x direction. Applying the integral operator of Eq. (21) on Eq. (20), and approximating the transverse leakage terms of the resulting equation by their node-edge spatial average, we obtain

$$\begin{aligned}\mu_m \frac{d}{dx}\widetilde{\Psi}_m^j(x) + \sigma_t^{ij}\widetilde{\Psi}_m^j(x) &= \frac{1}{4}\sum_{n=1}^{M}\sigma_s^{ij}\omega_n\widetilde{\Psi}_n^j(x)\\ &\quad - \frac{\eta_m}{h_{y_j}}[\widehat{\Psi}_m^{i,j+1} - \widehat{\Psi}_m^{i,j}]\\ &\quad + Q^{ij}, m = 1:M, (x,y)\\ &\quad \in \Gamma_{ij} \quad .\end{aligned} \tag{23}$$

An analogous procedure can be applied using the integral operator of Eq. (22).

To obtain the general solution of Eq. (23) in node Γ_{ij}, define $\widetilde{\Psi}_m^j(x) = \widetilde{\Psi}_m^{H_j}(x) + \widetilde{\Psi}_m^{P_j}(x)$, where superscripts H and P denote the homogeneous and the particular components of the general solution, respectively. For the homogeneous component, consider the transverse leakage terms and source term equal to zero. Now, a spectral analysis can be evaluated over the resulting equation considering $\widetilde{\Psi}_m^{H_j}(x) = a_m(\lambda)f_\lambda(x)$, where

$$f_\lambda(x) = \begin{cases} e^{-\lambda(x-x_i)}, & \text{if } \lambda > 0\\ e^{-\lambda(x-x_{i+1})}, & \text{if } \lambda < 0 \end{cases} \quad . \tag{24}$$

Over those conditions, Eq. (23) results in the following eigenvalue problem:

$$\frac{\sigma_t^{ij}}{\mu_m}a_m(\lambda) - \frac{1}{4\mu_m}\sum_{n=1}^{M}\sigma_s^{ij}\omega_n a_n(\lambda) = \lambda a_m(\lambda) \tag{25}$$

for $m = 1:M$. In Eq. (25), $a_n(\lambda)$ are the components of the eigenvector corresponding to the eigenvalue λ. The homogeneous solution is a linear combination of those eigenfunctions, i.e.,

$$\widetilde{\Psi}_m^{H_j}(x) = \sum_{l=1}^{M}\alpha_l a_m(\lambda_l)f_{\lambda_l}(x) \quad , \tag{26}$$

where α_l are arbitrary constants.

To determine the particular component of the general solution, we solve the linear system, which is obtained by the substitution of Ψ_{ij}^P into Eq. (23) for $m = 1:M$. In other words, the particular component is determined by the solution of the following system:

$$\widetilde{\boldsymbol{\Psi}}_{ij}^P = \boldsymbol{\Lambda}^{-1}\left[\boldsymbol{Q}_{ij} - \boldsymbol{I}_{\frac{\eta}{h_{y_j}}}(\widehat{\boldsymbol{\Psi}}_{i,j+1} - \widehat{\boldsymbol{\Psi}}_{i,j})\right] \quad , \tag{27}$$

where $\boldsymbol{\Lambda}$ = coefficient matrix originated from the linear system for the particular solution; $\boldsymbol{I}_{\frac{\eta}{h_{y_j}}} = M$-order diagonal matrix, such that $\boldsymbol{I}_{\frac{\eta}{h_{y_j}}} = diag\left[\frac{\eta_1}{h_{y_j}}, \frac{\eta_2}{h_{y_j}}, ..., \frac{\eta_M}{h_{y_j}}\right]$.

Therefore, the general solution of Eq. (23) is

$$\widetilde{\boldsymbol{\Psi}}_j(x) = \mathbf{A}\mathbf{F}_{f_\lambda}(x)\alpha + \widetilde{\boldsymbol{\Psi}}_{ij}^P \quad , \tag{28}$$

where $\widetilde{\boldsymbol{\Psi}}_j(x)$ = M-dimensional column vector composed of the node-edge angular fluxes along the y direction, i.e., $\widetilde{\boldsymbol{\Psi}}_j(x) = [\widetilde{\Psi}^j_1(x)\ \ \widetilde{\Psi}^j_2(x)\ \ ...\ \ \widetilde{\Psi}^j_M(x)]^T$ with T being the transpose; $\mathbf{A}$ = square matrix of order M, whose columns are the eigenvectors with components $a_m(\lambda)$; $\boldsymbol{F}_{f_\lambda(x)}$ = diagonal matrix of order M, whose nonzero entries are the functions $f_{\lambda_l}(x)$; α = length-M column vector whose components are arbitrary constants; $\widetilde{\boldsymbol{\Psi}}^P_{ij}$ is given by Eq. (27).

Now that an expression for the general solution was obtained, the focus is to build an expression that allows the estimation of the angular fluxes in the outgoing directions of a node based on the angular fluxes in the incoming directions. To illustrate that, we present in Fig. 5 a schematic illustration of the angular fluxes in the incoming and outgoing directions of a node Γ_{ij}. The dotted vectors in Fig. 5 represent the angular fluxes in the incoming directions d_i of node Γ_{ij}, and the solid vectors represent the angular fluxes in the outgoing directions of node Γ_{ij}.

In accordance with Fig. 5, we can write from Eq. (28) the relation $\widetilde{\boldsymbol{\Psi}}^{in}_j = \boldsymbol{M}\alpha + \widetilde{\boldsymbol{\Psi}}^P_{ij}$, where $\widetilde{\boldsymbol{\Psi}}^{in}_j = [\widetilde{\Psi}^{d_1}_{ij}\ \widetilde{\Psi}^{d_2}_{i+1,j}\ \widetilde{\Psi}^{d_3}_{i+1,j}\ \widetilde{\Psi}^{d_4}_{i,j}]^T$, with $\widetilde{\boldsymbol{\Psi}}^{d_k}_{ij}$, $k = 1:4$ being a set of vectors of order $M/4$ representing the incoming fluxes with direction d_k at the boundaries of Γ_{ij}. Matrix $\boldsymbol{M}$ is the product of $\boldsymbol{AF}_{f_\lambda}(x)$ over the respective x_i and x_{i+1}.

Notice that α can be written as $\alpha = \boldsymbol{M}^{-1}(\widetilde{\boldsymbol{\Psi}}^{in}_j - \widetilde{\boldsymbol{\Psi}}^P_{ij})$. Then, substituting the expression obtained for α into Eq. (28), it is possible to define an expression for the exiting fluxes in terms of the incoming fluxes, i.e.,

$$\widetilde{\boldsymbol{\Psi}}^{ex}_j = \widetilde{\boldsymbol{R}}\widetilde{\boldsymbol{\Psi}}^{in}_j + (\boldsymbol{I} - \widetilde{\boldsymbol{R}})\boldsymbol{\Lambda}^{-1}[\boldsymbol{Q}_{ij} - \boldsymbol{I}_{\frac{\eta}{h_{y_j}}}(\widehat{\boldsymbol{\Psi}}_{i,j+1} - \widehat{\boldsymbol{\Psi}}_{i,j})]\ , \tag{29}$$

where $\widetilde{\boldsymbol{R}}$ = M-order matrix, which is the product of $\mathbf{A}\mathbf{F}_{f_\lambda}(x)$ and $\boldsymbol{M}^{-1}$; $\boldsymbol{I}$ = identity matrix of order M.

Using an analogous procedure is possible to formulate an expression to compute the node-edge average angular fluxes along the x-coordinate direction making use of the node-edge angular fluxes in the incoming directions. That is,

$$\widehat{\boldsymbol{\Psi}}^{ex}_i = \widehat{\boldsymbol{R}}\widehat{\boldsymbol{\Psi}}^{in}_i + (\boldsymbol{I} - \widehat{\boldsymbol{R}})\boldsymbol{\Lambda}^{-1}[\boldsymbol{Q}_{ij} - \boldsymbol{I}_{\frac{\mu}{h_{x_i}}}(\widetilde{\boldsymbol{\Psi}}_{i+1,j} - \widetilde{\boldsymbol{\Psi}}_{i,j})]\ . \tag{30}$$

Equations (29) and (30) are the discretized equations of the RM-CN method applied to two-dimensional S_N transport problems. Combined, these equations are used to implement iterative schemes such as the Partial Node-Block-Inversion (Partial NBI) iterative scheme. The Partial NBI scheme uses the boundary conditions and the most recent estimates available for the node-edge angular fluxes in the incoming directions to evaluate the outgoing fluxes that constitute the incoming fluxes for the adjacent nodes in the directions of the transport sweeps. More details on the Partial NBI iterative scheme can be found in Ref. [24].

VI. NUMERICAL RESULTS

This section presents numerical results concerning four different problems. In the first problem (Sec. VI.A),

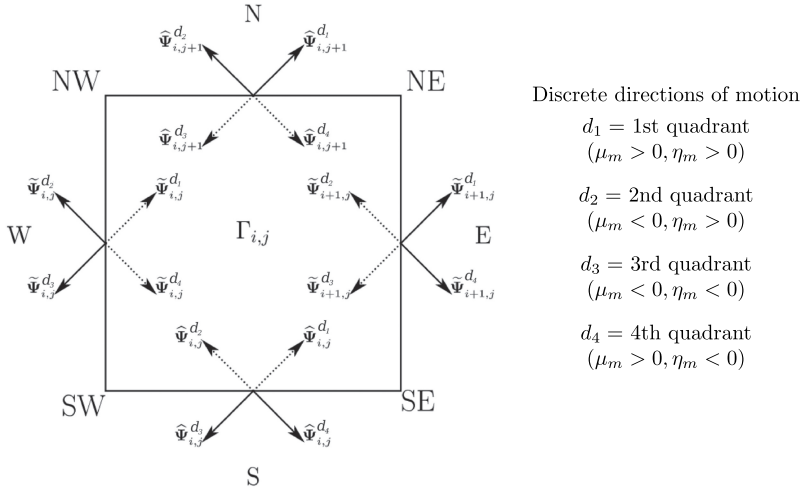


Fig. 5. Schematic illustration of the node-edge average angular fluxes in the incoming direction (dashed lines) and outgoing direction (solid lines) of node Γ_{ij}. Adapted from Ref. [24].

we present a homogeneous test case with the idea of evaluating the correctness and performance of the computer code implementing the Nyström method. In Sec. VI.B, three different heterogeneous problems are presented, showing results involving a new problem and problems already reported in the literature. Those results are compared with the ones reported and results generated from the RM-CN method to verify the accuracy of the presented integral method. All results presented in this section were generated by computer programs written in the C++ programming language, on a computer with an Intel Core i7-4820K, 3.7 GHz (four cores and eight threads) and 64 Gbytes of RAM, using double-precision floating-point data.

Problems presented in this section have a similar domain to that shown in Fig. 1. That is, they are composed of four regions R_i $(i = 1:4)$, where the internal source is embedded in region R_1. The size and cross sections of the regions can vary depending on the problem. Furthermore, for all problems, vacuum boundary conditions apply on the right and top boundaries of the domain, and reflective boundary conditions apply on the left and bottom boundaries of the domain. Also, the Gauss-Legendre quadrature was used in all problems presented here.

By convention, the units of measurement adopted are the length of the domain, measured in centimeters; the source, measured in neutron/cm^3·s; Φ, measured in neutron/cm^2·s; σ_s and σ_t, measured in inverse centimeters.

VI.A. Homogeneous Problem

This particular section presents a homogeneous case scenario, which has been chosen to test and assess the performance capabilities of the computer program implementing the Nyström method. This evaluation is important for understanding how the computer program behaves under consistent and uniform conditions, thereby providing valuable insights into its efficiency and reliability.

VI.A.1. Case I

This homogeneous problem was set by Tsai and Loyalka.[3] The domain is a square of unitary length, $a = b = 1$ cm, with a spatially uniform source $Q = 1$ neutron/cm^3·s embedded into region R_1. Region R_1 is a square region of length equal to 0.52 cm, i.e., $a_s = b_s = 0.52$ cm according to Fig. 1. In addition, $\sigma_t = 1.0$ cm^{-1}, and two values for the scattering macroscopic cross sections were considered.

This problem was also studied in several works such as those of Altaç and Spinrad[26] using SK_N and Altaç and Tekkalmaz[27] using $N - SK_N$. However, they present numerical results with accuracy of only one or two decimal places or present the numerical results in graphs, which makes numerical comparisons difficult. Moreover, none of the studies that analyzed this problem presented results for the average scalar flux in each region.

For this problem, the number of subregions N_R range from 2 to 20. Here, the scalar flux is computed for a mesh of points accounting for more than 40.000 points for the simple case of $N_R = 2$ and a total of approximately 130.000 points for $N_R = 20$. The precise calculation of scalar flux at discrete mesh points, rather than employing an averaged approach, affords significant benefits for hybrid, adjoint, and inverse problems, providing a benchmark alternative for those.

Tables I and II display numerical results for the scalar flux evaluated for $\sigma_s = 0.1$ and 0.9 cm^{-1}, respectively. For the first one, those were evaluated for $x = y = 0.5$ cm, $x = y = 0.7$ cm, and $x = y = 0.98$ cm and were compared with the results presented by Tsai and Loyalka.[3] Tables I and II also present the average scalar flux in each region that composed the domain for comparison with the results generated by the RM-CN method.

The results are in agreement with those presented by the papers of others and with the RM-CN method in, at least, three decimal places. It is also observed that when running the simplest problem, with $N_R = 2$, three decimal places of precision are obtained. Thus, a large number of subregions are needed only when greater precision is desired.

Regarding CPU time, Table III presents the computational time for each of the cases studied. Note that the processing time for the case with scattering equal to 0.9 cm^{-1} is always greater than the other problems. This is because each of the terms of the Neumann series is always multiplied by powers of σ_s; see Eq. (17). Thus, as the number of terms increases, the exponent increases, and the smaller the σ_s value is, the faster the series converges. However, when $\sigma_s = 0.9$ cm^{-1}, the coefficient does not decrease as fast as $\sigma_s = 0.1$ cm^{-1} as the number of terms increases; thus, a greater number of terms is needed for convergence. In this case, 15 terms were needed for the case where $\sigma_s = 0.1$ cm^{-1} and 30 terms for $\sigma_s = 0.9$ cm^{-1}.

To visually represent the distribution of scalar flux across the domain, we plotted it as contour lines for both problems, as shown in Fig. 6. Figures 6a and 6b present the scalar flux for Case I with $\sigma_s = 0.1$ cm^{-1} and $\sigma_s =$

TABLE I

Scalar Flux at Specific Spatial Points and the Average of Flux in Each Region of Case I with $\sigma_s = 0.1$ cm^{-1}

Region	$N_R = 2$	$N_R = 4$	$N_R = 10$	$N_R = 20$	Tsai and Loyalka[3]	RM-CN Method
$x = 0.5$[a]	2.5872e-1[b]	2.5850e-1	2.5840e-1	2.5866e-1	2.5891e-1	—
$x = 0.7$	8.2670e-2	8.2671e-2	8.2675e-2	8.2670e-2	8.2774e-2	—
$x = 0.98$	3.2612e-2	3.2612e-2	3.2612e-2	3.2612e-2	3.2622e-2	—
R_1[c]	4.6504e-1	4.6504e-1	4.6504e-1	4.6505e-1	—[d]	4.6319e-1
R_2 and R_3	1.4088e-1	1.4088e-1	1.4087e-1	1.4087e-1	—	1.4112e-1
R_4	7.0404e-2	7.0405e-2	7.0405e-2	7.0405e-2	—	7.2127e-1

[a]$y = x$ cm.
[b]Read as 2.5872×10^{-1} neutrons/cm^2·s.
[c]Region-average scalar flux.
[d]These data are not presented in the article.

TABLE II

Region-Average Scalar Flux in Each Region of Case I with $\sigma_s = 0.9$ cm^{-1}

Region	$N_R = 2$	$N_R = 4$	$N_R = 10$	$N_R = 20$	RM-CN Method
R_1	9.2161e-1[a]	9.2162e-1	9.2164e-1	9.2165e-1	9.1936e-1
R_2 and R_3	3.9384e-1	3.9385e-1	3.9385e-1	3.9385-1	3.9363e-1
R_4	2.2943e-1	2.2943e-1	2.2943e-1	2.2944e-1	2.3080e-1

[a]Read as 9.2161×10^{-1} neutrons/cm^2·s.

TABLE III

CPU Time for Different Numbers of Subregions for Case I

σ_s (cm^{-1})	$N_R = 2$	$N_R = 4$	$N_R = 10$	$N_R = 20$
0.1	15 min	23 min	70 min	7.5 h
0.9	28 min	42 min	140 min	13 h

0.9 cm^{-1}, respectively. Note that the scalar flux decreases faster in the first problem than in the last. This is due to the difference in the scattering macroscopic cross section between both problems.

In addition, Fig. 7 presents the value of the scalar flux in the diagonal of the domain for different values of σ_s. It is possible to observe an inflection in the flux when $x = 0.52$ cm because from then on, the points are outside the source region and the flux is influenced mainly by the particles that leave it. This shows that the method and the code are consistent with the physics of the problem in the homogeneous case.

VI.B. Heterogeneous Problems

In this section, four heterogeneous problems with different sizes are discussed.

VI.B.1. Case II

The initial problem examined in this study is a heterogeneous version of the previous case. This problem aims to analyze the efficiency of the method when maintaining a small domain, similar to Case I, while considering regions with different material parameters.

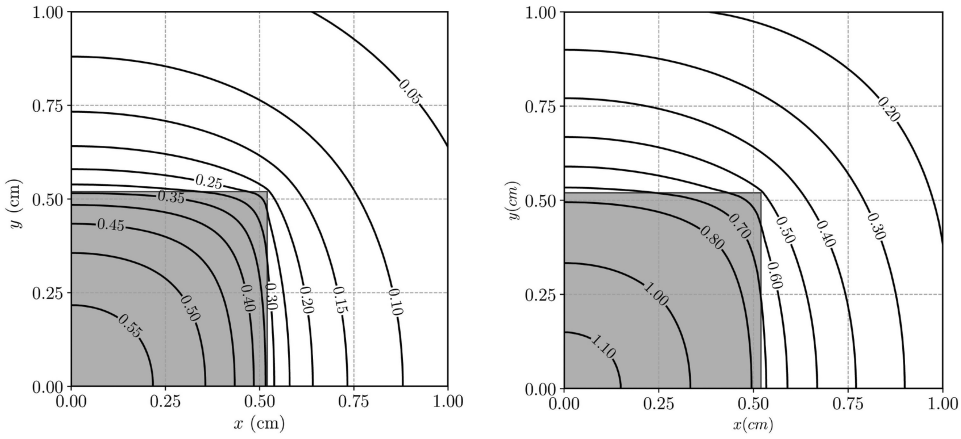


Fig. 6. Distribution of scalar flux along the domain for both problems in Case I: (a) $\sigma_s = 0.1$ cm^{-1} and (b) $\sigma_s = 0.9$ cm^{-1}.

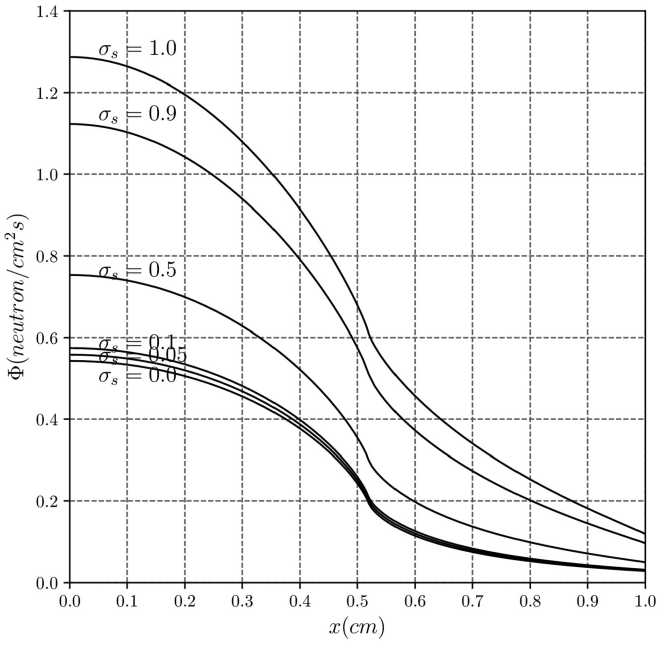


Fig. 7. Scalar flux of Case I for several values of σ_s.

The domain is a square of unitary length, $a = b =$ 1 cm, and a unit spatially uniform source embedded into region R_1. In Case II, different from Case I, we have $\sigma_t = 0.5$ cm^{-1} and $\sigma_s = 0.3$ cm^{-1} in region R_1 and $\sigma_t = 1.0$ cm^{-1} and $\sigma_s = 0.1$ cm^{-1} for regions R_2, R_3, and R_4.

The numerical results for this problem were compared with those generated by the RM-CN method. Table IV presents the region-average scalar flux for each region of the domain as the number of subregions increases.

As can be seen in Table IV, the code shows to be convergent, although it presents a small oscillation when compared with the result obtained using the RM-CN method. Above all, this problem shows that the code does not have programming defects independent of the input parameters.

VI.B.2. Case III

The second heterogeneous problem examined in this study was introduced by Azmy[1] and further explored by Mello and Barros,[28] as well as Barichello et al.[29,30] The goal of this problem is to analyze the efficiency of the method when extending the domain's size.

In this case, both the domain and the source region were extended equally in proportion. Thus, the total domain size and region R_1 increased such that $a = b = 10.0$ cm and $a_s = b_s = 5.0$ cm. In region R_1, $\sigma_t = 1$ cm^{-1} and $\sigma_s = 0.5$ cm^{-1}, while in the remaining regions, $\sigma_t = 2.0$ cm^{-1} and $\sigma_s = 0.1$ cm^{-1}.

Table V displays the region-average scalar flux for this problem as the number of subregions N_R increases. Comparative literature results were obtained using established methods: the Linear-Nodal method by Azmy and the ADO-Nodal method by Barichello et al. The results we obtained concur with those published by these researchers, demonstrating convergence with the increasing subdivision of regions.

Also, note that by choosing $N_R = 2$, it is already possible to ensure one to two decimal places of precision for three regions, with a low computational cost, on average 3 s. Subregions $N_R = 4$, $N_R = 10$, and $N_R = 20$ needed 1, 3, and 70 min, respectively, with 15 terms of the Neumann series.

Because of the scalar flux being close to zero in the region R_4, catastrophic cancellations may happen making

TABLE IV

Region-Average Scalar Flux in Each Region of Case II

Region	$N_R = 2$	$N_R = 4$	$N_R = 10$	$N_R = 20$	RM-CN Method
R_1	6.6953e-1[a]	6.7144e-1	6.7191e-1	6.7196e-1	6.6702e-1
R_2 and R_3	2.1066e-1	2.1089e-1	2.1064e-1	2.1060e-1	2.1043e-1
R_4	1.0762e-1	1.0770e-1	1.0771e-1	1.0771e-1	1.1052e-1

[a]Read as 6.6953×10^{-1} neutrons/cm^2·s.

TABLE V

Region-Average Scalar Flux for Each Region of Case III for Different Numbers of Subregions N_R

Region	$N_R = 2$	$N_R = 4$	$N_R = 10$	$N_R = 20$	Azmy[1]	Barrichello et al.[29]	RM-CN Method
R_1	1.6814	1.6836	1.6856	1.6857	1.676	1.6840	1.6839
R_2 and R_3	4.0134e-2[a]	4.0368e-2	4.1130e-2	4.0739e-2	4.159e-2	4.0663e-2	4.0698e-2
R_4	1.7516e-3	1.7605e-3	1.7705e-3	1.7726e-3	1.992e-3	1.8259e-3	1.8001e-3

[a]Read as 4.01345×10^{-2} neutrons/cm^2·s.

it extremely difficult to accurately compute exact values in that region. As can be seen in Fig. 8, the farther away from the source, the smaller the scalar flux is, which is physically expected. In addition, note that the decay in the scalar flux close to the source is relatively large, thus, along the domain, a large number of points has small values for the scalar flux, and numerical handling becomes complicated.

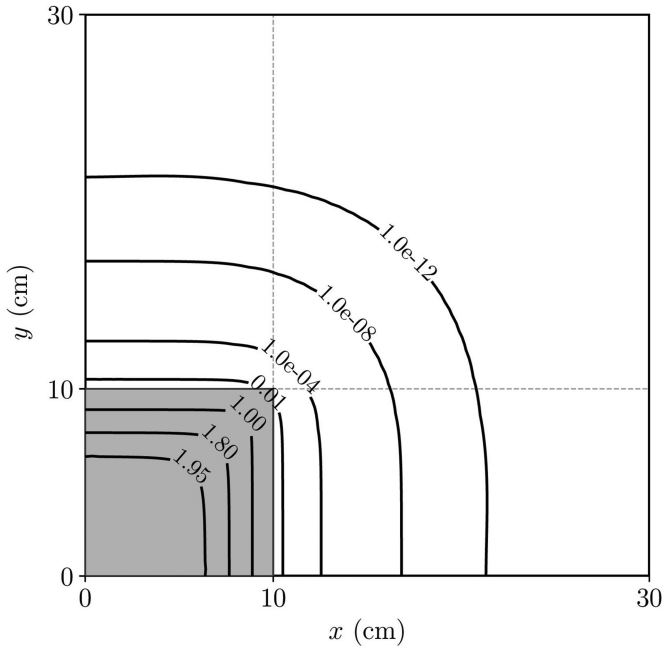


Fig. 8. Contour lines of the scalar flux for Case III.

Moreover, Fig. 8 provides insight into the distribution of scalar flux across the domain. Note that the flux distribution within the region R_1, where the neutron source is located, slowly decreases. As can be seen, close to the edge of the region R_1, the scalar flux is equal to 1.0 neutron/cm^2·s. However, just a few millimeters to the right, there is a sharp decay in a short distance, as it can be observed that the flux drops to 0.1 neutron/cm^2·s on the outside of the source and faster to 0.2 neutron/cm^2·s; from then on, the scalar flux decreases fast reaching values close to zero in a small distance. As the scalar flux approaches zero, catastrophic numerical cancellations can occur generating numerical instabilities.

In addition, note that the flux in regions R_2, R_3, and R_4 assume values close to zero, so any change in a point can cause noise in the calculation of the region-average scalar flux. Thus, precision in integrations and tabulations must be taken into account for this type of problem.

VI.B.3. Case IV

The fourth case maintains the same material parameters as the previous problem, but with different proportionality between the whole domain and region R_1. In this case, the region R_1 is 1/3 smaller than the domain. That is, $a = b = 30.0$ cm, and $a_s = b_s = 10.0$ cm. This problem aims to analyze the efficiency of the method when it is necessary to calculate the contribution of particles that travel long distances.

This problem is proposed by Barichello et al. in Ref. [29] to compare the accuracy of the solutions generated by the ADO-Nodal and AHOT-N0 methods. Table VI shows the region-average scalar flux for each region as a function of the considered discretization grid. As can be noticed from the results presented in Table VI, the offered method agreed up to two digits of precision for regions R_1, R_2, and R_3 and one digit of precision for region R_4 compared to the results given by Barichello et al. in Ref. [29] and those generated by the RM-CN method.

In addition, Fig. 9 provides the scalar flux distribution across the domain. Note that the average scalar flux is small for the regions outside region R_1 and that the flux outside of region R_1 decreases extremely fast. Thus, a numerical error in some points can cause noise in the average flux over all the regions.

The CPU times for each of the subregions described in Table VI were 15 min, 21 min, 1.1 h, and 4.2 h, respectively. Also, 15 terms of the Neumann series were needed to ensure convergence.

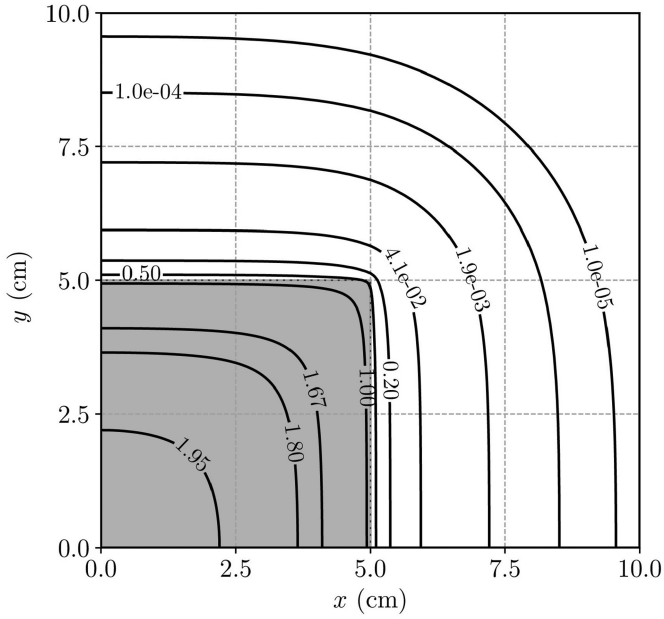


Fig. 9. Contour lines of the scalar flux for Case IV.

VII. CONCLUSION

In this work, the Nyström method was used to solve the steady-state, monoenergetic, X,Y-geometry neutron transport equation with isotropic scattering considering vacuum and reflective boundary conditions. The treatment of singularities of the integral formulation of the transport equation and the use of advanced computational packages were crucial to produce an accurate algorithm.

One conclusion found is that the provided code and methods are able to achieve a maximum of three decimal places of convergence. Additionally, we noted that in a smaller domain, the method exhibited good accuracy, especially considering that it calculates scalar flux at specific points rather than as an average, as in a typical discrete ordinates–based method. Another observation is that the Nyström method has the potential to be an interesting alternative to problems that require punctual results. However, in problems with larger domains, numerical difficulties arise, and catastrophic cancellations may occur.

Currently, work has been done to divide the singularity treatment into two parts—for values that are close to the singularity and for values that are distant to the singularity—in addition to the use of far-field techniques. The efficiency of handling singularities in homogeneous problems using the Nyström method, as shown in recent publications,[5,13,31] offers prospects for improving the quality of results in heterogeneous cases. Therefore, improvements both in the code and in the methodology are likely to yield more precise results. Preliminary studies are being carried out on this topic, and it is expected to be the subject of future works.

TABLE VI

Region-Average Scalar Flux in Each Region of Case IV

Region	$N_R = 2$	$N_R = 4$	$N_R = 10$	$N_R = 20$	Barichello et al.[29]	RM-CN Method
R_1	1.8341	1.8355	1.8379	1.8382	1.8360[a]	1.8360
R_2 and R_3	1.0438e-2[b]	1.0523e-2	1.0571e-2	1.0781e-2	1.0678e-2	1.0675e-2
R_4	1.0901e-4	1.0949e-4	1.0923e-4	1.1065e-4	1.1258e-4	1.1253e-4

[a]Results obtained using AHOT-N0 method.
[b]Read as 1.0438×10^{-2} neutrons/cm^2·s.

Acknowledgments

The authors acknowledge the financial support given by Coordenação de Aperfeiçoamento de Pessoal de Nível Superior (CAPES), Brazil.

Disclosure Statement

No potential conflict of interest was reported by the author(s).

Funding

This work was supported by the Conselho Nacional de Desenvolvimento Científico e Tecnológico; Coordenação de Aperfeiçoamento de Pessoal de Nível Superior.

ORCID

Gustavo A. Lorensi http://orcid.org/0000-0001-7176-9712
Leonardo R. C. Moraes http://orcid.org/0000-0001-5529-5422
Richard Vasques http://orcid.org/0000-0001-7021-7393
Esequia Sauter http://orcid.org/0000-0002-1697-2969
Fábio S. de Azevedo http://orcid.org/0000-0001-8992-2754

References

1. Y. AZMY, "Comparison of Three Approximations to the Linear-Linear Nodal Transport Method in Weighted Diamond-Difference Form," *Nucl. Sci. Eng.*, **100**, *3*, 190 (1988); https://doi.org/10.13182/NSE88-5.
2. L. B. BARICHELLO et al., "Recent Studies on the Asymptotic Convergence of the Spatial Discretization for Two-Dimensional Discrete Ordinates Solutions," *J. Comput. Theor. Transport*, **45**, *4*, 299 (2016); https://doi.org/10.1080/23324309.2016.1171242.
3. R. W. TSAI and S. K. LOYALKA, "Numerical Method for Solving Integral Equations of Neutron Transport: III," *Nucl. Sci. Eng.*, **61**, *4*, 536 (1976); https://doi.org/10.13182/NSE76-A14490.
4. S. K. LOYALKA and S. NAZ, "One Speed Black Sphere Problem: Some Benchmark Results," *Ann. Nucl. Energy*, **35**, *9*, 1774 (2008); https://doi.org/10.1016/j.anucene.2008.03.005.
5. F. S. AZEVEDO et al., "Integral Formulation and Numerical Simulations for the Neutron Transport Equation in X-Y Geometry," *Ann. Nucl. Energy*, **112**, 735 (2018); https://doi.org/10.1016/j.anucene.2017.10.017.
6. E. E. LEWIS and W. MILLER, *Computational Methods of Neutron Transport*, Wiley-Interscience, New York (1984).
7. L. B. BARICHELLO and C. E. SIEWERT, "A Discrete-Ordinates Solution for A Non-Grey Model with Complete Frequency Redistribution," *J. Quant. Spectrosc. Radiat. Transfer*, **62**, *6*, 665 (1999); https://doi.org/10.1016/S0022-4073(98)00096-X.
8. R. C. D. BARROS and E. W. LARSEN, "A Spectral Nodal Method for One-Group X, Y-Geometry Discrete Ordinates Problems," *Nucl. Sci. Eng.*, **111**, *1*, 34 (1992); https://doi.org/10.13182/NSE92-A23921.
9. K. D. LATHROP, "Ray Effects in Discrete Ordinates Equations," *Nucl. Sci. Eng.*, **32**, *3*, 357 (1968); https://doi.org/10.13182/NSE68-4.
10. Z. ALTAC and M. TEKKALMAZ, "Benchmark Solutions of Radiative Transfer Equation for Three-Dimensional Rectangular Homogeneous Media," *J. Quant. Spectrosc. Radiat. Transfer*, **109**, *4*, 587 (2008); https://doi.org/10.1016/j.jqsrt.2007.07.016.
11. S. K. LOYALKA and R. W. TSAI, "A Numerical Method for Solving Integral Equations of Neutron Transport—II," *Nucl. Sci. Eng.*, **58**, *2*, 193 (1975); https://doi.org/10.13182/NSE75-A28222.
12. L. LAZZARI, E. SAUTER, and F. S. DE AZEVEDO, "Simulation for Non-Homogeneous Transport Equation by Nyström Method," *Braz. J. Radiat. Sci.*, **8**, *3A* (2020).
13. C. BUBLITZ et al., "Numerical Results for Radiative Heat Transfer in Finite Cylindrical Medium with Isotropic Scattering," *J. Quant. Spectrosc. Radiat. Transfer*, **280**, 108087 (2022); https://doi.org/10.1016/j.jqsrt.2022.108087.
14. E. J. NYSTRÖM, "Über Die Praktische Auflösung von Integralgleichungen mit Anwendungen auf Randwertaufgaben," *Acta Mathematica*, **54**, *1*, 185 (1930); https://doi.org/10.1007/BF02547521.
15. G. A. LORENSI, E. SAUTER, and F. S. AZEVEDO, "Nyström Method Applied to the Two-Dimensional Transport Problem in Heterogeneous Medium," *Proc. Int. Conf. Mathematics and Computational Methods Applied to Nuclear Science and Engineering (M&C 2023)*, Niagara Falls, Canada, August 13–17, 2023, American Nuclear Society (2023).
16. P. J. OLVER et al., *Introduction to Partial Differential Equations*, Vol. 1, Springer (2014).
17. W. G. BICKLEY, "XXIV. Some Solutions of the Problem of Forced Convection," *Lond. Edinb. Dubl. Philos. Mag. J. Sci.*, **20**, *132*, 322 (1935); https://doi.org/10.1080/14786443508561482.
18. W. G. BICKLEY and J. NAYLER, "XXV. A Short Table of the Functions $Ki_n(x)$, from $n = 1$ to $n = 16$," *Lond. Edinb.*

Dubl. Philos. Mag. J. Sci., **20**, *132*, 343 (1935); https://doi.org/10.1080/14786443508561483.

19. K. YOSIDA, *Functional Analysis*, Springer-Verlag, Berlin (1966).
20. P. ANSELONE, "Singularity Subtraction in the Numerical Solution of Integral Equations," *ANZIAM J.*, **22**, *4*, 408 (1981).
21. M. WU et al., "Approximate Matrix Inversion for High-Throughput Data Detection in the Large-Scale MIMO Uplink," *Proc. 2013 Int. Symp. Circuits and Systems (ISCAS)*, May 19–23, 2013, p. 2155, IEEE (2013).
22. T. MATTSON and L. MEADOWS, "A 'Hands-On' Introduction to OpenMP," Intel Corporation (2014).
23. J. P. CURBELO et al., "The Modified Spectral Deterministic Method Applied to Fixed-Source Discrete Ordinates Problems in X, Y-Geometry," *Braz. J. Radiat. Sci.*, **8**, *3A* (2020).
24. O. P. DA SILVA et al., "A Response Matrix Spectral Nodal Method for Energy Multigroup X,Y-Geometry Discrete Ordinates Problems in Non-Multiplying Media," *Prog. Nucl. Energy*, **125**, 103288 (2020); https://doi.org/10.1016/j.pnucene.2020.103288.
25. L. R. C. MORAES et al., "A Response Matrix Method for Slab-Geometry Discrete Ordinates Adjoint Calculations in Energy-Dependent Neutral Particle Transport," *J. Comput. Theor. Transport*, **50**, *3*, 159 (2021); https://doi.org/10.1080/23324309.2021.1914661.
26. Z. ALTAC and B. I. SPINRAD, "The SK_N Method I: A High-Order Transport Approximation to Neutron Transport Problems," *Nucl. Sci. Eng.*, **106**, *4*, 471 (1990); https://doi.org/10.13182/NSE90-A23771.
27. Z. ALTAC and M. TEKKALMAZ, "Nodal Synthetic Kernel (N-SK_N) Method for Solving Neutron Transport Equation in One- and Two-Dimensional *X-Y* Geometries," *Ann. Nucl. Energy*, **64**, 320 (2014); https://doi.org/10.1016/j.anucene.2013.10.018.
28. J. A. M. DE MELLO and R. C. BARROS, "An Exponential Spectral Nodal Method for One-Speed X, Y-Geometry Deep Penetration Discrete Ordinates Problems," *Ann. Nucl. Energy*, **29**, *15*, 1855 (2002); https://doi.org/10.1016/S0306-4549(02)00013-0.
29. L. B. BARICHELLO, C. B. PICOLOTO, and R. D. DA CUNHA, "The ADO-Nodal Method for Solving Two-Dimensional Discrete Ordinates Transport Problems," *Ann. Nucl. Energy*, **108**, 376 (2017); https://doi.org/10.1016/j.anucene.2017.04.009.
30. L. B. BARICHELLO et al., "An Analytical Approach for a Nodal Formulation of a Two-Dimensional Fixed-Source Neutron Transport Problem in Heterogeneous Medium," *Kerntechnik*, **80**, *2*, 167 (2015); https://doi.org/10.3139/124.110468.
31. E. SAUTER, F. DE AZEVEDO, and P. KONZEN, "Nyström Method Applied to the Transport Equation in a Semi-Reflective Rectangle," *J. Comput. Theor. Transport*, **47**, *3*, 1 (2019).